nature materials

ARTICLES

PUBLISHED ONLINE: 17 NOVEMBER 2013 | DOI: 10.1038/NMAT3795

Enabling direct H_2O_2 production through rational electrocatalyst design

Samira Siahrostami[1†], Arnau Verdaguer-Casadevall[2†], Mohammadreza Karamad[1], Davide Deiana[3], Paolo Malacrida[2], Björn Wickman[2,4], María Escudero-Escribano[2], Elisa A. Paoli[2], Rasmus Frydendal[2], Thomas W. Hansen[3], Ib Chorkendorff[2], Ifan E. L. Stephens[2*] and Jan Rossmeisl[1*]

Future generations require more efficient and localized processes for energy conversion and chemical synthesis. The continuous on-site production of hydrogen peroxide would provide an attractive alternative to the present state-of-the-art, which is based on the complex anthraquinone process. The electrochemical reduction of oxygen to hydrogen peroxide is a particularly promising means of achieving this aim. However, it would require active, selective and stable materials to catalyse the reaction. Although progress has been made in this respect, further improvements through the development of new electrocatalysts are needed. Using density functional theory calculations, we identify Pt–Hg as a promising candidate. Electrochemical measurements on Pt–Hg nanoparticles show more than an order of magnitude improvement in mass activity, that is, A g^{-1} precious metal, for H_2O_2 production, over the best performing catalysts in the literature.

At present, the most commonly produced chemicals, such as ammonia, hydrogen, methanol and hydrogen peroxide are produced in centralized reactors on a very large scale. There is a general call[1,2] for a more decentralized infrastructure where both energy conversion and chemical synthesis are conducted closer to the point of consumption. Electrochemical devices are set to play an increasingly important role in reaching this goal; they can be operated under ambient conditions, at variable rates and require little auxiliary plant[3]. They can also be coupled with intermittent renewable power sources, such as solar or wind, providing a means to store electricity and level out demand. Herein, we focus on the electrochemical production of hydrogen peroxide.

Copious amounts of H_2O_2 are produced globally; its annual production exceeds 3 million tons (ref. 4). It is both an environmentally benign chemical oxidant, used for chemical synthesis, the pulp and paper industry and in water treatment[5,6], and a potential energy carrier[7]. When produced from H_2 and O_2, H_2O_2 production is exergonic, with a standard Gibbs free energy of formation, $\Delta G_f^0 = -120\,\mathrm{kJ\,mol^{-1}}$. At present, H_2O_2 is produced using the anthraquinone process, a batch method conducted in large-scale facilities, with an average yield of 50 thousand tons per year per plant[4]. It involves the sequential hydrogenation and oxidation of anthraquinone molecules, and it is energy intensive[8].

The inherent complexity of the anthraquinone process has motivated many researchers towards developing a direct synthesis of H_2O_2 from its elements,[9,10] aiming at: small-scale, continuous production through a catalytic process[6]. Pd-modified Au nanoparticles (henceforth denoted as Pd/Au) are the most active catalysts for this process[9]. The electroreduction of oxygen to H_2O_2 in a fuel cell or electrolyser holds significant advantages over the above processes. It would enable on-site production of hydrogen peroxide, and unlike the direct synthesis route, it would not be constrained by the need to maintain the hydrogen and oxygen outside the explosive regime. Moreover, when produced in a fuel cell, it should, in principle, be possible to recover most of the ΔG_f^0, 120 kJ mol^{-1}, as electrical energy. Alternatively, one could do away with H_2 altogether, and synthesize H_2O_2 at the cathode of an electrolyser; with oxygen evolution occurring at its anode, the energy input would be ~200 kJ mol^{-1} (see Supplementary Information). Nonetheless, industrially viable, electrochemical production of H_2O_2 requires a catalyst that is stable, active and selective for the electroreduction of oxygen[6,11–14].

The most active and selective catalysts found for this reaction, thus far, are based on porphyrins containing 3*d* transition metals such as Co (ref. 15). However, the nitrogen ligands of these catalysts degrade in the presence of H_2O_2, resulting in rapid performance losses[16,17]. On the other hand, catalysts based on noble metals provide adequate stability under the harsh reaction conditions. Au nanoparticles have a modest activity for H_2O_2 production, ~1 mA at 0.4 V overpotential, but with a selectivity of only ~80%. On the other hand, Pd/Au nanoparticles show similar activity to Au and up to ~90% selectivity[13]. An overview of different electrocatalysts for H_2O_2 production is shown in Fig. 1, compiled from the literature.

Here, our goal is to discover new alloys for the electrochemical generation of H_2O_2, exhibiting an unprecedented combination of activity, selectivity and stability. We specifically focus our attention on catalysts that function under ambient conditions, containing elements that are stable in acidic, rather than basic electrolytes. This is because H_2O_2 decomposes at high temperatures or alkaline conditions[6], and devices based on hydroxide-conducting polymeric electrolytes exhibit low membrane stability, poor water management and low hydrogen oxidation activity[18,19].

We identify the catalysts using density functional theory (DFT) calculations, synthesize and test them electrochemically and characterize their composition and structure *ex situ*.

[1]Center for Atomic-scale Materials Design, Department of Physics, Technical University of Denmark, DK-2800 Kongens Lyngby, Denmark, [2]Center for Individual Nanoparticle Functionality, Department of Physics, Technical University of Denmark, DK-2800 Kongens Lyngby, Denmark, [3]Center for Electron Nanoscopy, Technical University of Denmark, DK-2800 Kongens Lyngby, Denmark, [4]Department of Applied Physics, Chalmers University of Technology, SE-41296 Göteborg, Sweden. †These authors contributed equally to this work. *e-mail: ifan@fysik.dtu.dk; jross@fysik.dtu.dk

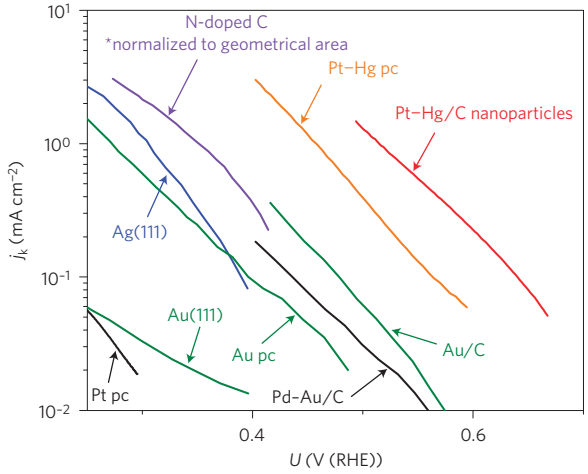

Figure 1 | Overview of different electrocatalysts for H_2O_2 production from the literature and from the present work. For the comparison, the kinetic current has been derived by correcting the partial current density for H_2O_2 production for mass transport limitations. Further details are available in the Methods and in the Supplementary Information. Data adapted from: ref. 46 for Pt polycrystalline (pc); ref. 47 for Au(111); ref. 48 for Au pc; ref. 49 for Ag(111); ref. 14 for N-doped C; ref. 13 for Pd–Au/C and Au/C. Data for Pt–Hg pc and Pt–Hg/C is from the present study.

Computational screening

The electroreduction of O_2 to H_2O_2 involves two coupled electron and proton transfers[20]:

$$O_2 + * + (H^+ + e^-) \rightarrow HOO^* \quad (1)$$

$$HOO^* + (H^+ + e^-) \rightarrow H_2O_2 + * \quad (2)$$

where $*$ denotes an unoccupied active site, and HOO* denotes the single adsorbed intermediate for the reaction. The catalyst provides high activity, by minimizing kinetic barriers for (1) and (2), and selectivity, by maximizing the barrier for HOO* reduction or dissociation to O* and OH*, the intermediates of the four-electron reduction of O_2 to H_2O.

The catalytic activity and selectivity, in turn, are determined by an interplay between two effects: ensemble effects and electronic effects. The binding of the reaction intermediates is controlled by electronic effects[21,22]. Varying the catalyst material allows one to tune the binding of HOO* to the surface. This means that the key parameter, or descriptor, in controlling the catalyst activity is the HOO* binding energy, ΔG_{HOO^*}. As the binding energy of HOO* scales linearly with that of HO*, ΔG_{HO^*} by a constant amount of 3.2 ± 0.2 eV (ref. 23), ΔG_{HO^*} can also be used as a descriptor. In Fig. 2e, the thermodynamic limiting potential, U_T, which is the most positive potential at which both (1) and (2) are downhill in free energy, is plotted, in blue, as a function of ΔG_{HO^*}; the HOO* binding energy is also shown on the upper horizontal axis for comparison. The thermodynamic overpotential for the two-electron reaction, η_{O_2/H_2O_2}, is denoted by the blue arrow, and is defined as the distance from the Nernstian potential for H_2O_2 production, $U^0_{O_2/H_2O_2} = 0.7$ V, to the U_T. Applying a bias equivalent to η_{O_2/H_2O_2} would allow the catalyst to sustain appreciable kinetic rates for H_2O_2 production, due to low charge transfer barriers[24–26].

Figure 2e establishes that there is a volcano-type relationship between η_{O_2/H_2O_2} (and hence the catalytic activity), and ΔG_{HO*}. Catalysts on the right-hand side of the volcano are limited by HOO* formation. For Au(211) it is 0.41 eV uphill to form HOO* at $U^0_{O_2/H_2O_2}$, as shown in the free-energy diagram in Fig. 2b. Accordingly, a thermodynamic overpotential of 0.41 V is required to drive the reaction. Catalysts on the left-hand side, such as Pt or Pd, bind HOO* too strongly, and the overpotential for the two-electron pathway is due to the reduction of HOO* to H_2O_2. The ideal catalyst, at the peak of the volcano, has a $\Delta G_{HOO*} \sim 4.2 \pm 0.2$ eV and $\eta_{O_2/H_2O_2} = 0$; its free-energy diagram is flat at the equilibrium potential, as shown in Fig. 2b. This means that the ideal catalyst would exhibit high current densities at negligible overpotentials.

In Fig. 2e, the U_T for the four-electron reduction of O_2 to H_2O is also plotted, in red, as a function of ΔG_{HO*} and ΔG_{HOO*}. In this case, there is an extra step contributing to the overpotential for the reaction, HO* reduction (where HO* is an adsorbed hydroxyl group, formed from the dissociation or reduction of HOO*; ref. 27):

$$HO^* + (H^+ + e^-) \rightarrow H_2O + * \quad (3)$$

The thermodynamic overpotential for equation (3), H_2O formation, η_{O_2/H_2O}, is indicated by the red arrow. Strikingly, in contrast to the two-electron volcano, even on the optimal catalyst, a minimum η_{O_2/H_2O} of ~0.4 V is required to drive H_2O formation.

The high value of η_{O_2/H_2O} is typical for reactions involving more than two electrons[20,22,23,26,28,29]; this is to overcome the large difference in adsorption energies between the intermediates, HO* and HOO*, whose binding energies scale linearly with each other[26]. On the other hand, the negligible overpotential required to drive O_2 reduction to H_2O_2 is characteristic of two-electron reactions, where the criterion for finding the ideal catalyst is relatively trivial: the adsorption of the sole reaction intermediate should be thermoneutral at the equilibrium potential[30].

The selectivity towards H_2O_2 or H_2O is determined by its propensity to break the O–O bond. This is, in turn, set by the binding strengths of the intermediates of the four-electron pathway, O* and HO*. To the left side of the peak (strong HO* binding) of both the four- and two-electron volcanoes (Fig. 2e), it is more downhill in free energy to form H_2O from HO*; this means the selectivity towards the four-electron pathway will dominate over the two-electron pathway, as is the case for Pt and Pd. The right side (weak HO* binding) of both two- and four-electron volcanoes overlap each other. In other words, at the peak of the two-electron volcano, there is a high activity for both H_2O_2 and H_2O formation, and both pathways will occur in tandem. Moving further right, beyond the peak of the two-electron volcano, towards Au it becomes more difficult to break the O–O bond and form HO* and O*, either through the chemical dissociation of HOO* or its electrochemical reduction. In summary, moving rightwards from the peak of the two-electron volcano weakens the interaction with O* and HO*, increasing the selectivity, but lowering the activity.

Apart from electronic effects, selectivity can also be controlled by geometric (or ensemble) effects; these are associated with the geometric arrangement of atoms on the catalyst surface[31,32]. On a selective catalyst, both the chemical dissociation to HO* and O* and the electrochemical reduction of HOO* to $O^* + H_2O$ should be avoided. Therefore, destabilizing O*, relative to HOO*, improves the selectivity. This can be achieved by controlling the geometry of the binding site: HOO* normally binds onto atop sites whereas O* binds onto hollow sites[33]. Eliminating hollow sites will specifically destabilize O*, without necessarily changing the activity. Catalysts such as Co-porphyrins[34] lack hollow sites whereas catalysts such as Pd/Au (ref. 13) contain hollow sites that interact weakly with oxygen; their active sites consist of single atoms, isolated by elements, such as Au, N or C (see Supplementary Information). This explains why Pd/Au is also an effective catalyst for the direct gas-phase synthesis of H_2O_2 from H_2 and O_2 (ref. 9).

Taking into account the above trends, using DFT, we screened for new alloy catalysts for the electrochemical generation of H_2O_2, which had not previously been tested. Our main criteria are that: for optimal activity, $\Delta G_{HOO*} \sim 4.2 \pm 0.2$ eV; each of the constituent

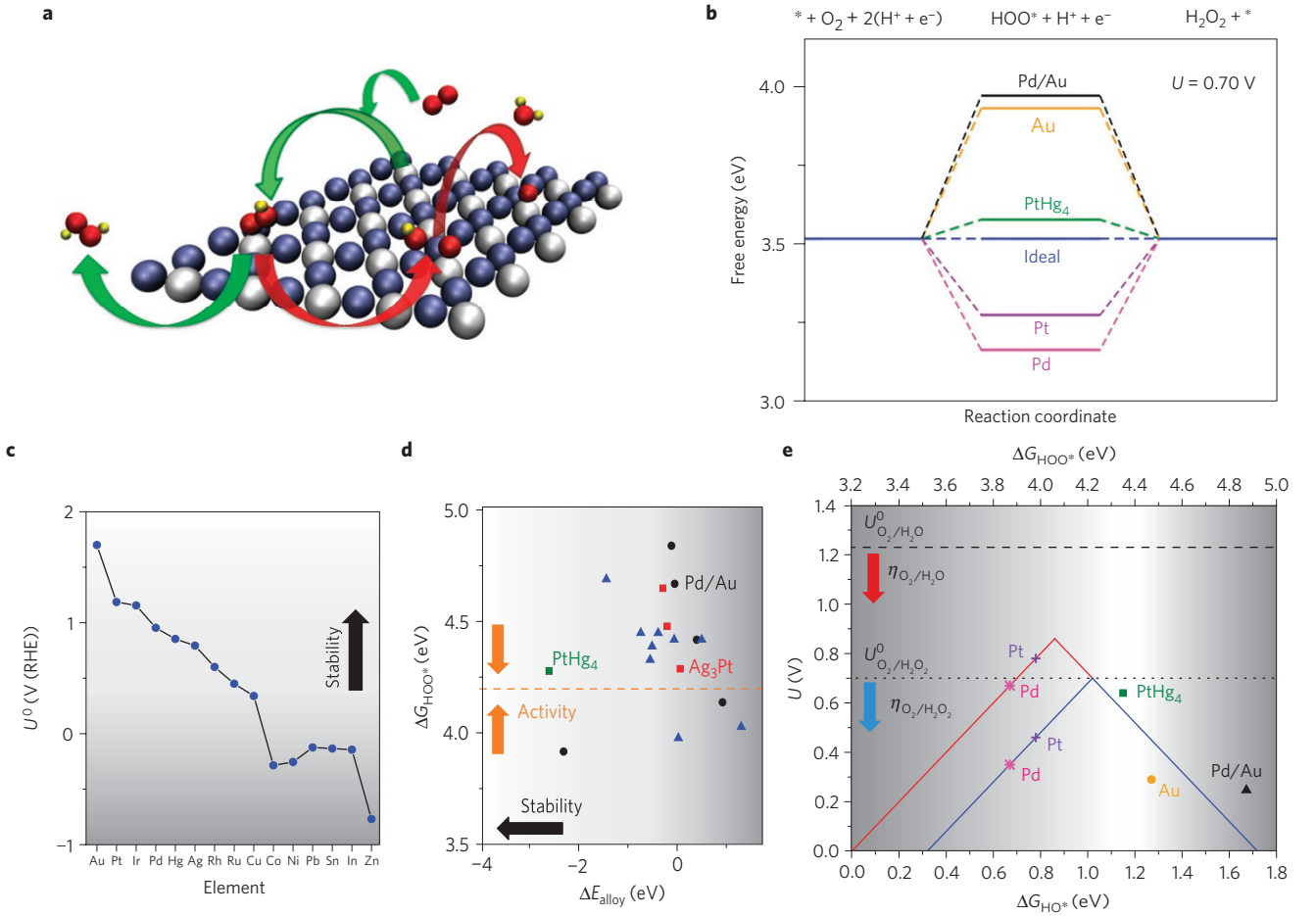

Figure 2 | Theoretical modelling of oxygen reduction to H_2O and H_2O_2. a, Representation of the $PtHg_4$(110) surface, based on the investigation of Hg/Pt(111) in ref. 35. The green arrows represent the reaction path to H_2O_2, whereas the red arrows the path to H_2O. Mercury, blue; platinum, grey; oxygen, red; hydrogen, yellow. **b**, Free-energy diagram for oxygen reduction to H_2O_2. The ideal catalyst is compared with $PtHg_4$(110), Pd/Au and closely packed pure metals Pd(111) and Au(211), all calculated for this work, and Pt(111), adapted from ref. 27. **c**, Dissolution potential for various elements under standard conditions[50]. **d**, Formation energy (per formula unit) ΔE_{alloy}, as a function of ΔG_{HOO*}. The optimal value for HOO binding is plotted as the orange dashed line. Bulk alloys are shown by red and green squares, surface alloys with a Au substrate are shown as black circles and surface alloys with non-Au substrate are shown by blue triangles. For **c**,**d** the colour gradient scales with stability, with the most stable areas highlighted in white. **e**, Theoretically calculated oxygen reduction volcano plot for the two-electron (blue) and four-electron (red) reduction of O_2, with the limiting potential plotted as a function of ΔG_{HO*} (lower horizontal axis) and ΔG_{HOO*} (upper horizontal axis). The equilibrium potential for the two-electron pathway, $U^0_{O_2/H_2O_2}$, is shown as the dotted line, and the equilibrium potential for the four-electron pathway, $U^0_{O_2/H_2O}$, is shown as the dashed line. The range of interesting HO* free energy for high selectivity and activity is highlighted with the greyscale gradient at its edges, recognizing limitations to the accuracy of DFT. Extensive details of the alloys included in the DFT screening are included in the Supplementary Information.

elements should be stable against dissolution or oxidation under reaction conditions; and the alloy should have as negative a heat of formation as possible (this provides a driving force to form the required monatomic ensembles). Each of the alloys has an active site where isolated atoms of the reactive metal, for example Pt, Pd, Rh or Ir, are surrounded by more inert elements, such as Au and Hg. A total number of 30 alloys were screened. An outline for the screening process is given in Fig. 2, (further details are available in the Supplementary Information).

Our attention was focused on the use of Hg as a means of forming the isolated reactive atoms. Hg is catalytically inactive. It is stable against dissolution up to 0.80 V at pH 0 (at standard conditions), and according to both our calculations (see Supplementary Information) and experiments[35] it forms stable alloys. The negative enthalpy of formation of the formed phase, $PtHg_4$, will stabilize the Hg, relative to pure Hg, meaning that it will be stable against dissolution. Hg can be easily electrodeposited onto Pt (ref. 36); on Pt(111) it forms a self-organized surface structure at room temperature[35]; each Pt atom is surrounded by Hg, as shown in Fig. 2a, thus forming the monatomic ensembles required for high selectivity. Figure 2b also shows that $PtHg_4$ has a close to optimal binding energy, with a thermodynamic overpotential smaller than 0.1 V. Alloying evidently induces electronic effects, as the binding of HOO* is ~0.37 eV weaker than pure Pt. Indeed, we emphasize that $PtHg_4$ is the only catalyst identified in the screening that fulfils all of our criteria for activity, selectivity and stability.

Although Hg is toxic, only monolayer quantities of Hg would be required to produce the required atomic ensembles; its present industrial applications, for example, lighting or the cathode for chlorine synthesis, require much larger amounts[4]. In the following we show that $PtHg_4$ is indeed highly selective and active for the two-electron pathway.

Experimental results

To synthesize $PtHg_4$, we modified a polycrystalline Pt disc following the procedure of ref. 35 for Hg/Pt(111). About 10 monolayers

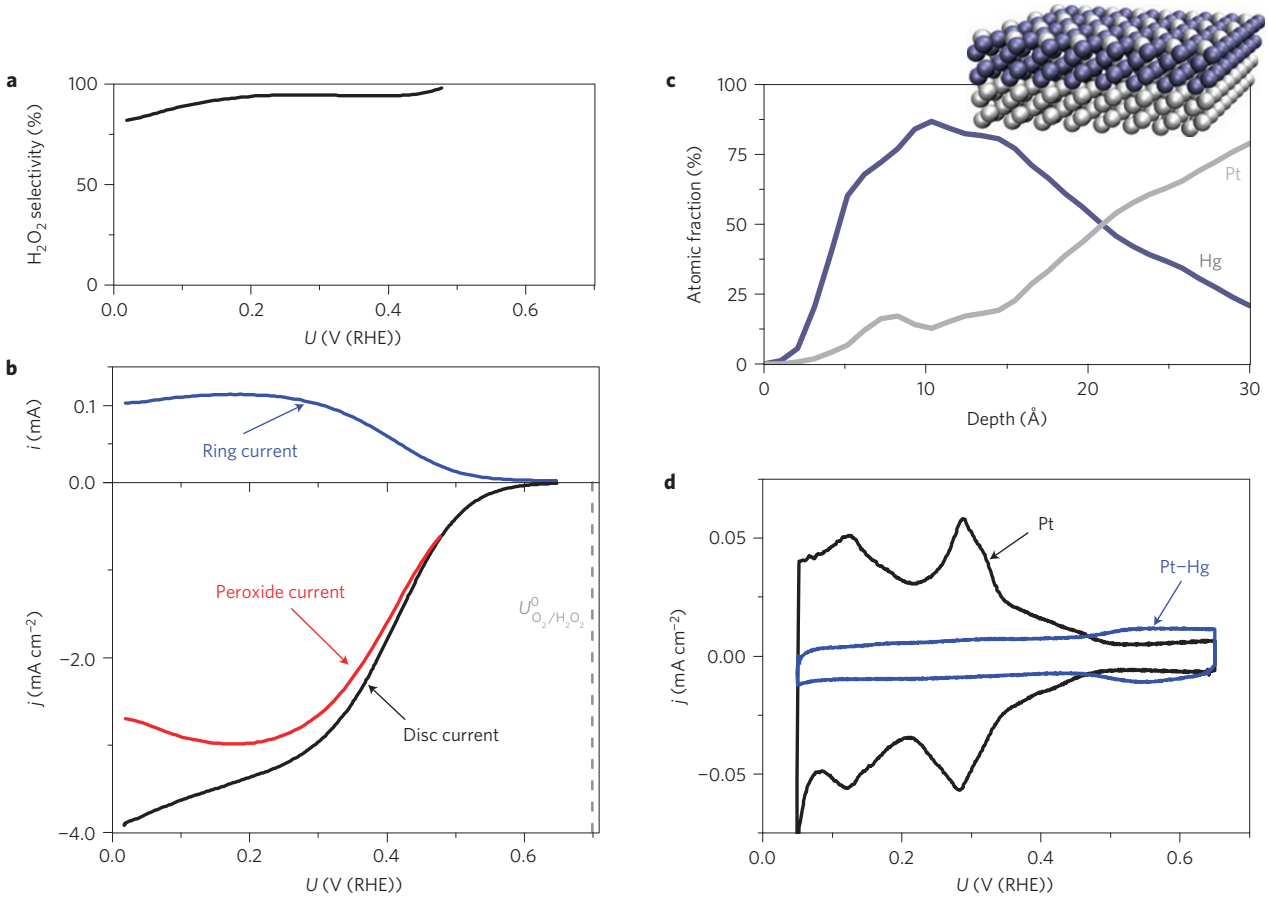

Figure 3 | Experimental characterization of Pt–Hg on extended surfaces. a, H_2O_2 selectivity as a function of the applied potential. **b**, RRDE voltammograms at 1,600 r.p.m. in O_2-saturated electrolyte with the disc current, ring current and current corresponding to hydrogen peroxide obtained from the ring current (only the anodic cycle is shown). **c**, Angle-resolved XPS depth profile of Pt–Hg. The adventitious C and O traces have been omitted for clarity. The inset shows a schematic representation of the structure revealed by the angle-resolved depth profile, with a Pt–Hg alloy above a Pt substrate. **d**, Voltammograms in N_2-saturated electrolyte of Pt and Pt–Hg. All electrochemical measurements were taken in 0.1 M $HClO_4$ and at 50 mV s^{-1} at room temperature.

of Hg were electrodeposited from $HgClO_4$. *Ex situ* angle-resolved X-ray photoelectron spectroscopy (XPS) of the sample at this stage revealed that the surface is composed of ~20% Pt and ~80% Hg, in agreement with a $PtHg_4$ structure (Fig. 3c). Figure 3d shows a cyclic voltammogram in N_2-saturated solution for Pt and Hg-modified Pt. The voltammogram for Pt shows the typical hydrogen adsorption/desorption peaks at 0.05–0.5 V, whereas Pt–Hg has a flat profile, suggesting a negligible amount of hydrogen adsorption. This is consistent with our DFT calculations (see Supplementary Information), which show that H is destabilized on $PtHg_4$(110), relative to Pt(111). Moreover, isolated Pd atoms on Au exhibit similar voltammograms[13]. We understand this phenomenon on the basis that on pure Pt and Pd, H usually adsorbs at hollow sites, with three Pt or Pd nearest neighbours[37]; isolated Pt or Pd atoms would lack such sites. The negative alloying energy of $PtHg_4$ provides a driving force to maximize the coordination of Hg to Pt and minimize the number of Pt–Pt nearest neighbours. Further evidence for the surface composition can be found in the Supplementary Information. In summary, our observations support the notion that isolated Pt atoms are formed at the surface of Pt–Hg, consistent with earlier experiments on Hg/Pt(111) (ref. 35).

We measure the electrochemical activity for oxygen reduction to hydrogen peroxide, using the rotating ring disc electrode (RRDE) technique[38]. Figure 3b shows the voltammograms in oxygen for Pt–Hg. The disc current increases exponentially with a decrease in potential from ~0.6 V, as kinetic barriers are lowered. To quantify the amount of hydrogen peroxide formed, the ring was potentiostated at 1.2 V, where the oxygen reduction current is negligible and H_2O_2 oxidation is mass transport limited. This gives rise to a positive current at the ring as hydrogen peroxide is produced at the disc (Fig. 3b). The onset potential at the ring and the disc coincide at ~0.6 V, corresponding to an overpotential of ~0.1 V. Such low overpotential is in agreement with our theoretical predictions. As the overpotential increases, most of the current in the disc can be accounted for by the amount of H_2O_2 detected at the ring; the efficiency of hydrogen peroxide production is as high as 96% in the region between 0.2 and 0.4 V (Fig. 3a). Within these potential limits, the hydrogen peroxide current density is 3 mA cm^{-2}, the theoretical mass transport limit for the two-electron reduction of oxygen. It is only at potentials below 0.2 V that both selectivity and hydrogen peroxide current start to decrease, implying that water formation is favoured.

To validate the stability criteria for our computational screening (Fig. 2), we also tested Pt–Sn and Ag_3Pt as catalysts for H_2O_2 production. As described in the Supplementary Information, we predict that both of these catalysts would, in principle, have optimal H_2O_2 activity. However, they fail to meet our stability criteria. Consequently, the less noble component, Sn or Ag, dissolved under reaction conditions. These examples illustrate the importance of stability in the corrosive electrochemical environment, which is both acidic and oxidizing.

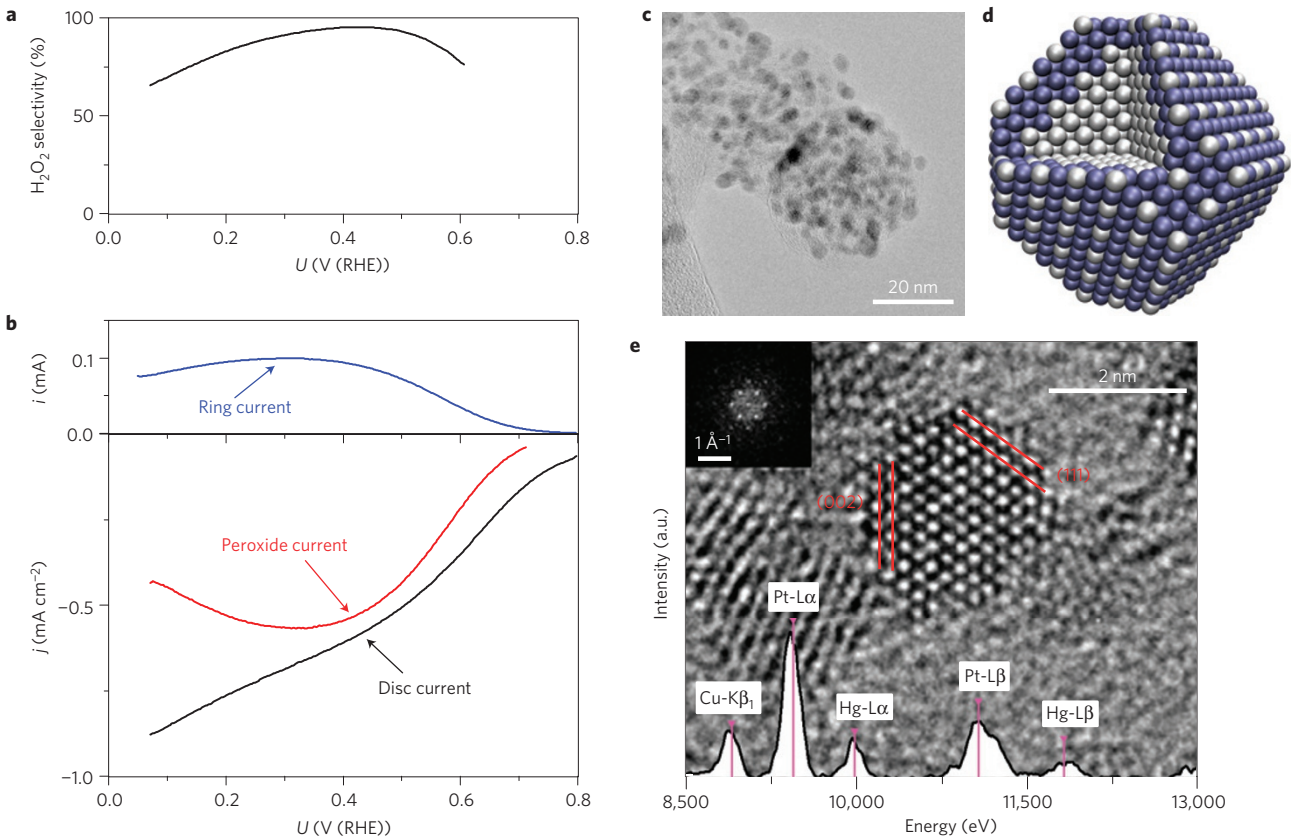

Figure 4 | Experimental characterization of Pt–Hg/C nanoparticles. a, H_2O_2 selectivity as a function of the applied potential. **b**, RRDE voltammograms at 1,600 r.p.m. in O_2-saturated electrolyte with the disc current, ring current and current corresponding to hydrogen peroxide obtained from the ring current (only the anodic cycle is shown). All electrochemical measurements were taken in 0.1 M $HClO_4$ and at 50 mV s^{-1} at room temperature. The disc current is normalized to the surface area of Pt nanoparticles (from H-upd) before deposition of Hg. **c**, TEM image of Pt–Hg/C nanoparticles. **d**, Schematic representation of a Pt–Hg/C nanoparticle. Mercury, blue; platinum, grey. **e**, HRTEM image of a single Pt–Hg nanoparticle, with the corresponding EDS spectrum of the particle superimposed on top, with peaks corresponding to Pt and Hg from the nanoparticle, and Cu, from the TEM grid; the {111} and {002} planes are shown in red; the corresponding diffractogram is shown in the inset.

Ultimately, should electrochemical hydrogen peroxide synthesis make a technological impact, it will require high-surface-area catalysts or thin films[26,39]. It turns out that Pt–Hg/C nanoparticles are even more active than the extended surfaces.

An ink was prepared from commercial Pt/C and drop-cast on a glassy carbon electrode (details in the Supplementary Information). To prepare the Pt–Hg alloy we followed the same electrodeposition procedure as for the polycrystalline surface. The features of the base voltammograms were similar to those of polycrystalline Pt–Hg (see Supplementary Information).

Transmission electron microscopy (TEM) analysis showed well-distributed nanoparticles on the carbon support (Fig. 4c). A high-resolution TEM (HRTEM) image of a single nanoparticle and its Fourier transform are shown in Fig. 4e. By positioning the scanning TEM probe on an individual nanoparticle, an energy-dispersive X-ray spectroscopy (EDS) spectrum as shown in Fig. 4e was acquired. Both Pt and Hg peaks are present in the spectrum. XPS analysis, which is sensitive to the first few atomic layers, confirmed the presence of both elements. However, the lattice parameters from the HRTEM are consistent with the structure of Pt. Together, the HRTEM and XPS data suggest a core of Pt and a shell of Pt–Hg (see Supplementary Information).

We then evaluated oxygen reduction on Hg-modified Pt nanoparticles (Fig. 4b), where we observed a similar current profile to the polycrystalline surfaces. The ring current proved that a high yield of hydrogen peroxide was achieved, with over 90% selectivity between 0.3 and 0.5 V (Fig. 4a). The catalyst is highly stable under reaction conditions. When cycling the potential between 0.05 and 0.8 V for 8,000 cycles in an O_2-saturated electrolyte, there were no measurable losses in H_2O_2 production activity (see Supplementary Information).

The viability of an electrochemical device producing H_2O_2 will require it to be efficient, safe and that the cost of its constituent materials is minimal. Given that the most viable catalysts for H_2O_2 production are based on precious metals, it is essential that the loading of these metals is minimized, that is, that the current density per gram of precious metal is maximized.

State-of-the-art fuel cells and electrolysers are engineered to avoid losses due to the transport of oxygen. Thus, to yield a quantitative comparison of catalyst performance, we have corrected the data in Figs 3 and 4 for mass transport losses. The results are shown in Fig. 1. In terms of specific activity (normalized to the surface area of Pt), nanoparticulate Pt–Hg/C exhibits 4–5 times the activity of polycrystalline Pt–Hg. The higher activity of the nanoparticles compared with extended surfaces indicates that undercoordinated sites, which are more prevalent on nanoparticulate surfaces[40], could play an important role in the reaction. Notably, Pt–Hg/C shows more than one order of magnitude improvement in mass activity over previously reported Pd–Au/C or Au/C (ref. 13). To the best of our knowledge, Pt–Hg nanoparticles present the best activity reported in the literature for hydrogen peroxide synthesis on a metallic catalyst, with a selectivity of up to 96% and a mass activity of $26 \pm 4\ A\ g^{-1}_{noble\ metal}$ at 50 mV overpotential.

In this work, we have taken advantage of the isolated active site concept to tune the activity and selectivity for oxygen reduction. Our theoretical model successfully predicted Pt–Hg as an active, selective and stable catalyst for hydrogen peroxide synthesis.

Comparing the activity reported here with that reported for other two-electron reactions, we anticipate that it should be possible to discover even more active catalysts for electrochemical H_2O_2 production[23,30,37,41,42]. Nonetheless, as our theoretical model shows, improved activity may come at the cost of selectivity. The rational approach used here to tune activity and selectivity can be extended to other, more complex reactions for sustainable energy conversion, in particular the electroreduction of CO_2 and N_2 (refs 28,29).

Methods

Computational details. The computational analysis was carried out using grid-based projector-augmented wave (GPAW) method, a DFT code based on a projected augmented wave (all-electron frozen core approximation) method integrated with the atomic simulation environment[43,44]. The revised Perdew–Burke–Ernzerhof functional was used as an exchange correlation functional[45]. An eight-layer 2×2 slab with 17.5 Å vacuum between successive slabs was used to model the $PtHg_4(110)$ surface. Monkhorst–Pack grids with dimensions of $4 \times 4 \times 1$ were used to sample the Brillouin zone. The bottom four layers were fixed in the bulk structure whereas the upper layers and adsorbates were allowed to relax in all directions until residual forces were less than 0.05 eV $Å^{-1}$. Further details on DFT calculations are provided in the Supplementary Information.

Extended surface electrode preparation. A platinum polycrystalline electrode was mirror polished to <0.25 μm before every experiment and prepared by flame annealing as previously reported[46]. Several voltammograms in nitrogen-saturated 0.1 M $HClO_4$ were recorded to ensure a reproducible surface, and then the electrode was moved to an electrodeposition cell containing 0.1 M $HClO_4$ + 1 mM $HgClO_4$. The potential was swept from open circuit (about 1 V) at 50 mV s^{-1} to 0.2 V, where the potential was stopped for 2 min to electrodeposit mercury following the procedure detailed in ref. 35. The potential was scanned to 0.65 V at 50 mV s^{-1} and stopped there while removing the electrode from the cell. We immediately moved the Hg-modified Pt electrode back into the RRDE cell, where it was inserted under potential control of about 0.1 V in N_2-saturated 0.1 M $HClO_4$. Then the potential was swept between 0.05 and 0.65 V until a stable cyclic voltammogram was obtained. As we observed mercury traces at the ring, we cleaned it electrochemically by cycling it between 0.05 and 1.6 V while rotating the electrode to avoid mercury redeposition. Once the ring and disc voltammetries became stable, we saturated the cell with O_2 to record voltammetries at the disc while keeping the ring at 1.2 V to detect H_2O_2.

High-surface-area catalysts. To prepare the Pt/C nanoparticles, a simple synthesis method was employed. First, 5.75 mg of 60% wt Pt supported on C was mixed with 9.5 ml of Millipore water, 3 ml of isopropanol and 50 μl of 1:100 Nafion. To facilitate dispersion of the nanoparticles, 20 μl of 2% wt solution of polyvinylpyrrolidone was used. The nanoparticles had a nominal size of 3 nm. The mixture was sonicated for 20 min at about 25 °C and 10 μl of it was drop-casted on top of a glassy carbon disc of 0.196 cm^2. The sample was then left to dry before embedding into a RRDE set-up. To ensure a good dispersion of the film, oxygen reduction was carried out on the Pt/C nanoparticles (see Supplementary Information). The same procedure adopted for the polycrystalline sample was followed to electrodeposit mercury. All data relative to nanoparticles were normalized to the underpotential deposition of hydrogen (H-upd; that is, assuming that the voltammetric charge between 0.5 and 0.05 V is equivalent to 210 μC cm^{-2} of Pt surface area[18]) before Hg deposition, and the corresponding capacitance was subtracted from all oxygen reduction measurements.

Chemicals. Concentrated $HClO_4$ was obtained from Merck and diluted to 0.1 M. $HgClO_4$ was obtained from Sigma Aldrich and diluted in 0.1 M $HClO_4$ to reach 1 mM $HgClO_4$. All gases were of 5N5 quality and purchased from AGA.

Electrochemical measurements. A typical three-electrode cell was used for the RRDE experiments. Another three-electrode cell was used to electrodeposit mercury. In both cells the counter electrodes were Pt wires and Hg/Hg_2SO_4 electrodes were used as a reference, separated from the working electrode compartment using a ceramic frit. All potentials are quoted with respect to the reversible hydrogen electrode, and are corrected for ohmic losses. All experiments were performed using a Bio-Logic Instruments' VMP2 potentiostat, controlled by a computer. The RRDE assembly was provided by Pine Instruments Corporation. The ring was made of platinum and its collection efficiency, N, was of 20 ± 1%. To compute H_2O_2 selectivity, η, we made use of the following equation[38]: $\eta = 2(I_r/N)/(I_d + I_r/N)$, where I_r and I_d are ring and disc currents, respectively. H_2O_2 selectivity is not calculated below ~0.2 mA of disc current, owing to a poorer signal to background ratio at low currents.

To correct the current for mass transport losses, the equation $1/j = 1/j_d + 1/j_k$ was used, where j is the total current, j_d is the mass-transport-limited current to hydrogen peroxide (obtained from the ring), and j_k is the kinetic current to hydrogen peroxide. Further details are given in the Supplementary Information.

Received 27 June 2013; accepted 1 October 2013; published online 17 November 2013; corrected after print 21 November 2013 and 23 December 2013

References

1. Perlo, P. *et al. Catalysis for Sustainable Energy Production* 89–105 (Wiley, 2009).
2. Armaroli, N. & Balzani, V. The future of energy supply: challenges and opportunities. *Angew. Chem. Int. Ed.* **46,** 52–66 (2007).
3. Kotrel, S. & Brauninger, S. in *Handbook of Heterogeneous Catalysis* 2nd edn (eds Ertl, G., Knoezinger, H., Schueth, F. & Weitkamp, J.) 1963 (Wiley, 2008).
4. *Ullmann's Encyclopedia of Industrial Chemistry* (Wiley, 1999–2013).
5. Samanta, C. Direct synthesis of hydrogen peroxide from hydrogen and oxygen: An overview of recent developments in the process. *Appl. Catal. A* **350,** 133–149 (2008).
6. Campos-Martin, J. M., Blanco-Brieva, G. & Fierro, J. L. G. Hydrogen peroxide synthesis: An outlook beyond the anthraquinone process. *Angew. Chem. Int. Ed.* **45,** 6962–6984 (2006).
7. Fukuzumi, S., Yamada, Y. & Karlin, K. D. Hydrogen peroxide as a sustainable energy carrier: Electrocatalytic production of hydrogen peroxide and the fuel cell. *Electrochim. Acta* **82,** 493–511 (2012).
8. Hâncu, D., Green, J. & Beckman, E. J. H_2O_2 in CO_2/H_2O biphasic systems: Green synthesis and epoxidation reactions. *Ind. Eng. Chem. Res.* **41,** 4466–4474 (2002).
9. Edwards, J. K. *et al.* Switching off hydrogen peroxide hydrogenation in the direct synthesis process. *Science* **323,** 1037–1041 (2009).
10. Ford, D. C., Nilekar, A. U., Xu, Y. & Mavrikakis, M. Partial and complete reduction of O_2 by hydrogen on transition metal surfaces. *Surf. Sci.* **604,** 1565–1575 (2010).
11. Yamanaka, I., Hashimoto, T., Ichihashi, R. & Otsuka, K. Direct synthesis of H_2O_2 acid solutions on carbon cathode prepared from activated carbon and vapor-growing-carbon-fiber by a H_2/O_2 fuel cell. *Electrochim. Acta* **53,** 4824–4832 (2008).
12. Lobyntseva, E., Kallio, T., Alexeyeva, N., Tammeveski, K. & Kontturi, K. Electrochemical synthesis of hydrogen peroxide: Rotating disk electrode and fuel cell studies. *Electrochim. Acta* **52,** 7262–7269 (2007).
13. Jirkovský, J. S. *et al.* Single atom hot-spots at Au–Pd nanoalloys for electrocatalytic H_2O_2 Production. *J. Am. Chem. Soc.* **133,** 19432–19441 (2011).
14. Fellinger, T-P., Hasché, F., Strasser, P. & Antonietti, M. Mesoporous nitrogen-doped carbon for the electrocatalytic synthesis of hydrogen peroxide. *J. Am. Chem. Soc.* **134,** 4072–4075 (2012).
15. Gouérec, P. & Savy, M. Oxygen reduction electrocatalysis: Ageing of pyrolyzed cobalt macrocycles dispersed on an active carbon. *Electrochim. Acta* **44,** 2653–2661 (1999).
16. Bezerra, C. W. B. *et al.* A review of Fe–N/C and Co–N/C catalysts for the oxygen reduction reaction. *Electrochim. Acta* **53,** 4937–4951 (2008).
17. Schulenburg, H. *et al.* Catalysts for the oxygen reduction from heat-treated iron(III) tetramethoxyphenylporphyrin chloride: Structure and stability of active sites. *J. Phys. Chem. B* **107,** 9034–9041 (2003).
18. Sheng, W., Gasteiger, H. A. & Shao-Horn, Y. Hydrogen oxidation and evolution reaction kinetics on platinum: Acid vs alkaline electrolytes. *J. Electrochem. Soc.* **157,** B1529–B1536 (2010).
19. Ayers, K. E., Dalton, L. T. & Anderson, E. B. Efficient generation of high energy density fuel from water. *ECS Trans.* **41,** 27–38 (2012).
20. Viswanathan, V., Hansen, H. A., Rossmeisl, J. & Nørskov, J. K. Unifying the 2e– and 4e– reduction of oxygen on metal surfaces. *J. Phys. Chem. Lett.* **3,** 2948–2951 (2012).
21. Norskov, J. K., Bligaard, T., Rossmeisl, J. & Christensen, C. H. Towards the computational design of solid catalysts. *Nature Chem.* **1,** 37–46 (2009).
22. Greeley, J. *et al.* Alloys of platinum and early transition metals as oxygen reduction electrocatalysts. *Nature Chem.* **1,** 552–556 (2009).
23. Koper, M. T. M. Thermodynamic theory of multi-electron transfer reactions: Implications for electrocatalysis. *J. Electroanal. Chem.* **660,** 254–260 (2011).
24. Janik, M. J., Taylor, C. D. & Neurock, M. First-principles analysis of the initial electroreduction steps of oxygen over Pt(111). *J. Electrochem. Soc.* **156,** B126–B135 (2009) doi:10.1149/1.3008005.
25. Tripković, V., Skúlason, E., Siahrostami, S., Nørskov, J. K. & Rossmeisl, J. The oxygen reduction reaction mechanism on Pt(111) from density functional theory calculations. *Electrochim. Acta* **55,** 7975–7981 (2010).
26. Stephens, I. E. L., Bondarenko, A. S., Gronbjerg, U., Rossmeisl, J. & Chorkendorff, I. Understanding the electrocatalysis of oxygen reduction on platinum and its alloys. *Energy Environ. Sci.* **5,** 6744–6762 (2012).
27. Rossmeisl, J., Karlberg, G. S., Jaramillo, T. & Norskov, J. K. Steady state oxygen reduction and cyclic voltammetry. *Faraday Discuss.* **140,** 337–346 (2009).

28. Peterson, A. A. & Nørskov, J. K. Activity descriptors for CO_2 electroreduction to methane on transition-metal catalysts. *J. Phys. Chem. Lett.* **3,** 251–258 (2012).
29. Skulason, E. *et al.* A theoretical evaluation of possible transition metal electro-catalysts for N_2 reduction. *Phys. Chem. Chem. Phys.* **14,** 1235–1245 (2012).
30. Hansen, H. A. *et al.* Electrochemical chlorine evolution at rutile oxide (110) surfaces. *Phys. Chem. Chem. Phys.* **12,** 283–290 (2010).
31. Maroun, F., Ozanam, F., Magnussen, O. M. & Behm, R. J. The role of atomic ensembles in the reactivity of bimetallic electrocatalysts. *Science* **293,** 1811–1814 (2001).
32. Strmcnik, D. *et al.* Enhanced electrocatalysis of the oxygen reduction reaction based on patterning of platinum surfaces with cyanide. *Nature Chem.* **2,** 880–885 (2010).
33. Viswanathan, V. *et al.* Simulating linear sweep voltammetry from first-principles: Application to electrochemical oxidation of water on Pt(111) and Pt3Ni(111). *J. Phys. Chem. C* **116,** 4698–4704 (2012).
34. Siahrostami, S., Bjorketun, M. E., Strasser, P., Greeley, J. & Rossmeisl, J. Tandem cathode for proton exchange membrane fuel cells. *Phys. Chem. Chem. Phys.* **15,** 9326–9334 (2013).
35. Wu, H. L., Yau, S. & Zei, M. S. Crystalline alloys produced by mercury electrodeposition on Pt(111) electrode at room temperature. *Electrochim. Acta* **53,** 5961–5967 (2008).
36. Angerstein-Kozlowska, H., MacDougall, B. & Conway, B. E. Origin of activation effects of acetonitrile and mercury in electrocatalytic oxidation of formic acid. *J. Electrochem. Soc.* **120,** 756–766 (1973).
37. Skuílason, E. *et al.* Modeling the electrochemical hydrogen oxidation and evolution reactions on the basis of density functional theory calculations. *J. Phys. Chem. C* **114,** 18182–18197 (2010).
38. Paulus, U. A., Schmidt, T. J., Gasteiger, H. A. & Behm, R. J. Oxygen reduction on a high-surface area Pt/Vulcan carbon catalyst: A thin-film rotating ring-disk electrode study. *J. Electroanal. Chem.* **495,** 134–145 (2001).
39. Van der Vliet, D. F. *et al.* Mesostructured thin films as electrocatalysts with tunable composition and surface morphology. *Nature Mater.* **11,** 1051–1058 (2012).
40. Perez-Alonso, F. J. *et al.* The effect of size on the oxygen electroreduction activity of mass-selected platinum nanoparticles. *Angew. Chem. Intl Ed.* **51,** 4641–4643 (2012).
41. Wesselmark, M., Wickman, B., Lagergren, C. & Lindbergh, G. Hydrogen oxidation reaction on thin platinum electrodes in the polymer electrolyte fuel cell. *Electrochem. Commun.* **12,** 1585–1588 (2010).
42. Wolfschmidt, H., Weingarth, D. & Stimming, U. Enhanced reactivity for hydrogen reactions at Pt nanoislands on Au(111). *ChemPhysChem* **11,** 1533–1541 (2010).
43. Mortensen, J. J., Hansen, L. B. & Jacobsen, K. W. Real-space grid implementation of the projector augmented wave method. *Phys. Rev. B* **71,** 035109 (2005).
44. Atomic Simulation Environment (ASE), available at https://wiki.fysik.dtu.dk/ase, Center for Atomic Scale Material Design (CAMD), Technical University of Denmark, Lyngby.
45. Hammer, B., Hansen, L. B. & Nørskov, J. K. Improved adsorption energetics within density-functional theory using revised Perdew-Burke-Ernzerhof functionals. *Phys. Rev. B* **59,** 7413–7421 (1999).
46. Verdaguer-Casadevall, A., Hernandez-Fernandez, P., Stephens, I. E. L., Chorkendorff, I. & Dahl, S. The effect of ammonia upon the electrocatalysis of hydrogen oxidation and oxygen reduction on polycrystalline platinum. *J. Power Sources* **220,** 205–210 (2012).
47. Alvarez-Rizatti, M. & Jüttner, K. Electrocatalysis of oxygen reduction by UPD of lead on gold single-crystal surfaces. *J. Electroanal. Chem. Interfacial Electrochem.* **144,** 351–363 (1983).
48. Jirkovsky, J. S., Halasa, M. & Schiffrin, D. J. Kinetics of electrocatalytic reduction of oxygen and hydrogen peroxide on dispersed gold nanoparticles. *Phys. Chem. Chem. Phys.* **12,** 8042–8053 (2010).
49. Blizanac, B. B., Ross, P. N. & Markovic, N. M. Oxygen electroreduction on Ag(111): The pH effect. *Electrochim. Acta* **52,** 2264–2271 (2007).
50. *CRC Handbook of Chemistry and Physics* (CRC Press, 1996).

Acknowledgements

The authors gratefully acknowledge financial support from the Danish Ministry of Science's UNIK initiative, Catalysis for Sustainable Energy and The Danish Council for Strategic Research's project NACORR (12-132695). M.E-E. acknowledges financial support from EU PF7's initiative Fuel Cell and Hydrogen Joint Undertaking's project CathCat (GA 303492). B.W. thanks Formas (project number 219-2011-959) for financial support. The Center for Individual Nanoparticle Functionality is supported by the Danish National Research Foundation (DNRF54).

Author contributions

J.R. and S.S. conceived the DFT calculations. S.S. and M.K. performed the DFT calculations. A.V. and I.E.L.S. designed the experiments. A.V. performed the electrochemical experiments, D.D. the TEM, P.M. the XPS and B.W. the EQCM and SEM-EDS. E.A.P. and R.F. prepared the Ag_3Pt sample and performed its XRD. S.S., A.V. and I.E.L.S. co-wrote the first draft of the paper. A.V. designed the figures. All authors discussed the results and commented on the manuscript.

Additional information

Supplementary information is available in the online version of the paper. Reprints and permissions information is available online at www.nature.com/reprints. Correspondence and requests for materials should be addressed to I.E.L.S. or J.R.

Competing financial interests

Patent application EP 13165265.3 'Alloy catalyst material' has been filed.

CORRIGENDUM

Enabling direct H_2O_2 production through rational electrocatalyst design

Samira Siahrostami, Arnau Verdaguer-Casadevall, Mohammadreza Karamad, Davide Deiana, Paolo Malacrida, Björn Wickman, María Escudero-Escribano, Elisa A. Paoli, Rasmus Frydendal, Thomas W. Hansen, Ib Chorkendorff, Ifan E. L. Stephens and Jan Rossmeisl

Nature Materials **12,** 1137–1143 (2013); published online 17 November 2013; corrected after print 21 November 2013.

In the version of this Article originally published, the middle initials of the penultimate author were missing; the name should have read Ifan E. L. Stephens. In the Author contributions and Additional information sections 'I.S.' should have read 'I.E.L.S.' These errors have now been corrected in the online versions of the Article.

ERRATUM

Enabling direct H_2O_2 production through rational electrocatalyst design

Samira Siahrostami, Arnau Verdaguer-Casadevall, Mohammadreza Karamad, Davide Deiana, Paolo Malacrida, Björn Wickman, María Escudero-Escribano, Elisa A. Paoli, Rasmus Frydendal, Thomas W. Hansen, Ib Chorkendorff, Ifan E. L. Stephens and Jan Rossmeisl

Nature Materials **12,** 1137–1143 (2013); published online 17 November 2013; corrected after print 21 November 2013 and 23 December 2013.

In the version of this Article originally published, in Fig. 1, the top two values on the *y* axis were switched. This error has now been corrected in the online versions of the Article.